Quantitative dental measurements by use of simultaneous frequency-domain laser infrared photothermal radiometry and luminescence

Lena Nicolaides, Chris Feng, Andreas Mandelis, and Stephen H. Abrams

Modulated (frequency-domain) infrared photothermal radiometry (PTR) is used as a dynamic quantitative dental inspection tool complementary to modulated luminescence (LM) to quantify sound enamel or dentin. A dynamic high-spatial-resolution experimental imaging setup, which can provide simultaneous measurements of laser-induced modulated PTR and LM signals from defects in teeth, has been developed. Following optical absorption of laser photons, the experimental setup can monitor simultaneously and independently the nonradiative (optical-to-thermal) energy conversion by infrared PTR and the radiative deexcitation by LM emission. The relaxation lifetimes (τ_1, τ_2) and optical absorption, scattering, and spectrally averaged infrared emission coefficients (μ_α, μ_s, $\bar{\mu}_{IR}$) of enamel are then determined with realistic three-dimensional LM and photothermal models for turbid media followed by multiparameter fits to the data. A quantitative band of values for healthy enamel with respect to these parameters can be generated so as to provide an explicit criterion for the assessment of healthy enamel and, in a future extension, to facilitate the diagnosis of the onset of demineralization in carious enamel. © 2002 Optical Society of America

OCIS codes: 260.3060, 260.3800.

1. Introduction

In recent years, rapidly growing research activities centered on laser-induced luminescence (LM) as a probing technique have been reported for the detection and quantification of physical and chemical processes associated with carious dental enamel.[1] In general, LM induced through continuous (dc) irradiation of dental tissue suffers from low signal levels, and thus in most cases dyes are used to enhance sensitivity.[2] Under laboratory conditions, the results appear satisfactory, yet use of dyes makes the method difficult for clinical applications. Much progress has been made with the introduction of another dc laser technique, which relies on long-lived fluorescence present in carious regions of the tooth that emit only in the red spectral region. This decay time and spectral characteristics are typical of metal-free porphyrin monomers.[3] The spectral characteristics were found to be typical of protoporphyrin IX, which may be present because of bacterial biosynthesis occurring within carious tissue.[4] There is also speculation that pigments present in specific foods or drinks may be responsible.[1]

Recently a combination of modulated frequency-domain (FD) laser-induced infrared photothermal radiometry (PTR) and modulated laser LM was introduced as a dynamic dental diagnostic tool to quantify sound enamel or dentin[5,6] as well as subsurface cracks in human teeth. Under 488-nm laser excitation it was found that radiometric images are complementary to LM images as a direct result of the complementary nature of nonradiative and radiative deexcitation processes, which are responsible for the complementary signal generation. It was also concluded qualitatively that radiometric images are depth profilometric. No definitive conclusions regarding the depth profilometric character of FD LM were reached. Finally, LM frequency responses from enamel and hydroxyapatite were found to exhibit two relaxation lifetimes, the longer of which (~ms) is common to all teeth (including canine) and is not sensitive to the defect state or the overall quality

L. Nicolaides, C. Feng, and A. Mandelis (mandelis@mie.utoronto.ca) are with the Photothermal and Optoelectronic Diagnostics Laboratories, Department of Mechanical and Industrial Engineering, University of Toronto, 5 King's College Road, Toronto, Ontario M5S 3G8, Canada. S. H. Abrams is with Four Cell Consulting, 748 Briar Hill Avenue, Toronto, Ontario M6B 1L3, Canada.

of the enamel. The shorter lifetime ($\lesssim \mu$s), however, can vary substantially from tooth to tooth, and preliminary results show that it is sensitive to the presence of caries. No quantitative model was advanced for the observed LM and PTR signals in the earlier studies.[5,6] PTR has the ability to penetrate and yield information about an optically absorbing or scattering medium at depths well below the range of optical imaging. As a result of this ability, pulsed-laser PTR has been used extensively with soft turbid media such as tissue[7,8] to study the subsurface deposition localization of laser radiation, a task that is difficult for optical methods because of excessive scattering. Unfortunately, the availability of a single-signal channel (transient decay) in pulsed PTR renders this technique difficult or impossible to use for quantitative measurements to uniquely derive both optical absorption and scattering coefficients of turbid media without additional independent measurements.[8] On the contrary, the availability of two signal channels (amplitude and phase) in FD PTR makes this technique optimally suitable for quantitative photothermal measurements of optical parameters of turbid (hard and soft) tissue. Indeed, it is of significant importance to ascertain the uniqueness of the PTR measurement parameters, a task that we undertake in this paper.

Our experimental FD method combination is based on low-fluence laser irradiation[5] and detects the simultaneous emission of infrared radiation and LM from a heated region of a turbid sample without thermally altering it. The technique has been used to perform the first quantitative measurements in dental enamel from several teeth. The method and the results are reported in this paper. A dentin–enamel interface was examined for quantitative comparison with enamel-generated signals. A theoretical model was then fitted to the enamel sample data, and a novel three-parameter computational algorithm was introduced to obtain a unique set of the optical properties of dental enamel. The three-dimensional LM and PTR models developed and used in this study are computationally intensive, yet necessary to account for radial and normal (depthwise) degrees of freedom of the optical and thermal-wave energy fluxes into the turbid medium (enamel and dentin) from focused laser sources.

2. Three-Dimensional Theoretical Luminescence and Photothermal Radiometry Models

LM and PTR frequency scans can be used for quantitative analysis and measurement of the optical properties of both enamel and dentin. A quantitative theoretical two-lifetime rate model of dental LM has been advanced to explain the two characteristic lifetimes (τ_1 and τ_2) in the 10-Hz to 10-kHz range observed with all human (and some canine) teeth tested so far to our knowledge under 488-nm laser excitation.[5,6] In a generalized theoretical model, the LM signal from a two-level excited-state system corresponding to independently acting dental chromophores (respective lifetimes τ_1 and τ_2) is

considered. The model allows for considerable depletion of the ground states. The total density of radiatively deexciting fluorophores that emit LM at angular modulation frequency ω is given by[5]

$$\rho(\omega) = \frac{N_{T_1}\tau_1}{W_1\tau_1 + 1 + i\omega\tau_1} + \frac{N_{T_2}\tau_2}{W_2\tau_2 + 1 + i\omega\tau_2}, \quad (1)$$

where N_{T_1} and N_{T_2} are the total populations of fluorophore manifolds 1 and 2, respectively. W_1 and W_2 are the optical pumping rates out of the two ground states, respectively. It follows that the source term for the PTR signal is

$$E_t = E_1 + E_2$$
$$= I_0 \left(\frac{E_{01}}{W_1\tau_1 + 1 + i\omega\tau_1} + \frac{E_{02}}{W_2\tau_2 + 1 + i\omega\tau_2} \right), \quad (2)$$

where E_{01} and E_{02} are the energies of excited levels 1 and 2 of the two fluorophores, respectively. I_0 is a constant corresponding to the incident laser intensity. The isotropic thermal-wave source in the presence of the total photon field density $\Psi_t(r, z; \omega)$ at the coordinate point $\mathbf{r} = (r, z)$ in a turbid medium is[8,9]

$$Q(r, z; \omega) = \eta_{NR}\mu_\alpha \Psi_t(r, z; \omega) E_t \quad \text{(W/m}^3\text{)}, \quad (3)$$

where $\eta_{NR}\mu_\alpha$ is the probability of one-photon loss that is due to nonradiative decay, η_{NR} is the nonradiative quantum yield, and μ_α is the optical absorption coefficient at the laser excitation wavelength. The total photon field density $\Psi_t(r, z; \omega)$ is the sum of diffuse and coherent terms[10,11]

$$\Psi_t(r, z; \omega) = \Psi_d(r, z; \omega) + \Psi_c(r, z; \omega), \quad (4)$$

where Ψ_d is the diffuse photon density and Ψ_c is the coherent photon density in the turbid medium. For a Gaussian laser beam of spot size W and incident power P, impinging on the surface of a turbid medium of reflectivity R, the coherent optical field is given by

$$\Psi_c(r, z; \omega) = [P(1 - R)/\pi W^2]\exp(-2r^2/W^2 - \mu_t z), \quad (5)$$

where

$$\mu_t \equiv \mu_\alpha + \mu_s. \quad (6)$$

Here μ_s is the optical scattering coefficient of the turbid medium. The diffuse photon density in the turbid medium is most conveniently expressed analytically as[7,12]

$$\nabla^2\psi_d(r, z; \omega) - 3\mu_\alpha\mu_t'\psi_d(r, z; \omega) = -\frac{1}{D} G(r, z; \omega), \quad (7a)$$

where

$$G(r, z; \omega) \equiv C_1(\omega) \exp(-2r^2/W^2 - \mu_t z); \quad (7b)$$

also

$$D = 1/3\mu_t' \quad (7c)$$

is the optical diffusion coefficient (in meters). Furthermore,

$$C_1(\omega) \equiv \frac{(1-R)P\mu_s}{2\pi W^2}\left(\frac{\mu_t + g\mu_\alpha}{\mu_t - g\mu_s}\right)[1 + \exp(i\omega t)],$$

(7d)

$$\mu_t' \equiv \mu_t - g\mu_s = \mu_\alpha + (1-g)\mu_s$$
$$= \mu_\alpha + \mu_s' \qquad (\mathrm{m}^{-1}),$$

(7e)

where g is the mean cosine of the scattering angle. Next, it is convenient to take the Hankel transform of $\psi_d(r, z; \omega)$:

$$\tilde{\phi}_d(z; \lambda, \omega) = \int_0^\infty \psi_d(r, z; \omega)J_0(\lambda r)r\mathrm{d}r,$$

(8)

where $J_0(x)$ is the Bessel function of the first kind of order zero. Equation (7a) is thus transformed to an ordinary differential equation:

$$\frac{\mathrm{d}^2}{\mathrm{d}z^2}\tilde{\phi}_d(z; \lambda, \omega) - \beta^2\tilde{\phi}_d(z; \lambda, \omega) = -\frac{1}{D}\tilde{G}(z; \lambda, \omega),$$

(9a)

where

$$\tilde{I}(\lambda, \omega) = \frac{P(1-R)}{2\pi W^2}\exp(i\omega t)$$
$$\times \int_0^\infty \exp(-2r^2/W^2)J_0(\lambda r)r\mathrm{d}r$$
$$= \frac{P(1-R)}{2\pi}\exp[-(\lambda^2 W^2/8) + i\omega t] \quad (11a)$$

is the Hankel transform of the radial optical source distribution $\psi_c(r, 0; \omega)$, Eq. (5). To complete the solution, the coherent photon density must be added to the diffuse photon density distribution, Eqs. (4) and (5). The Hankel transform of ψ_c is

$$\tilde{\phi}_c(z; \lambda, \omega) = \tilde{I}(\lambda, \omega)\exp(-\mu_t z).$$

(11b)

Solving the boundary-value problem of Eqs. (9a), (10a), and (10b) in Hankel space and adding the contributions that are due to the coherent field, we obtain the Hankel transform of the total photon density field in the turbid medium:

$$\tilde{\phi}(z; \lambda, \omega) = \tilde{\phi}_c(z; \lambda, \omega) + \tilde{\phi}_d(z; \lambda, \omega)$$
$$= \frac{[F_1 - \gamma F_2 \exp(-\beta L)]\exp(-\beta z) + [F_2 - \gamma F_1 \exp(-\beta L)]\exp[-\beta(L-z)]}{(1 + A\beta)[1 - \gamma^2 \exp(-2\beta L)]}$$
$$+ \left[1 - \frac{1}{D}\left(\frac{\mu_t + g\mu_\alpha}{\mu_t - g\mu_s}\right)\left(\frac{\mu_s}{\mu_t^2 - \beta^2}\right)\right]\exp(-\mu_t z)\tilde{I}(\lambda, \omega).$$

(12)

with

$$\beta^2(\lambda) \equiv \lambda^2 + (\mu_\alpha/D) \qquad (\mathrm{m}^{-2}),$$

(9b)

$$\tilde{G}(z; \lambda, \omega) \equiv C_1 W^2 \exp[-(\lambda^2 W^2)/8 - \mu_t z]$$
$$\times [1 + \exp(i\omega t)].$$

(9c)

Considering also the Hankel transform of the coherent field, Eq. (5) and use of the boundary-condition requirement that there should be no diffuse intensity entering the medium from outside,[9–11] the Hankel transforms of the boundary conditions are

$$\tilde{\phi}_d(0; \lambda, \omega) - A\frac{\mathrm{d}}{\mathrm{d}z}\tilde{\phi}_d(z; \lambda, \omega)\big|_{z=0}$$
$$= -3\mu_s gA\tilde{I}(\lambda, \omega),$$

(10a)

$$\tilde{\phi}_d(L; \lambda, \omega) + A\frac{\mathrm{d}}{\mathrm{d}z}\tilde{\phi}_d(z; \lambda, \omega)\big|_{z=L}$$
$$= 3\mu_s gA\exp(-\mu_t L)\tilde{I}(\lambda, \omega), \quad (10b)$$

Here the constants A and γ are given as follows:

$$A = 2D\left(\frac{1 + r_{21}}{1 - r_{21}}\right) \qquad (\mathrm{m}); \qquad \gamma \equiv \frac{1 - A\beta}{1 + A\beta}, \quad (13)$$

where r_{12} is the internal reflectance, defined as the ratio of the upward-to-downward hemispherical diffuse optical fluxes at the boundary.[13] This definition of A (in the normalized form $A \to A/2D$) has been used by Groenhuis et al.[14] along with an empirical relationship between r_{21} and the relative refractive index n_{21}. L is the thickness of the turbid medium. Furthermore, the following definitions were made:

$$F_1 = \left[\frac{1}{D}\left(\frac{1 + \mu_t A}{\mu_t^2 - \beta^2}\right)\left(\frac{\mu_t + g\mu_\alpha}{\mu_t - g\mu_s}\right) - \frac{2g}{\mu_t'}\right]\mu_s\tilde{I}(\lambda, \omega),$$

(14a)

$$F_2 = \left[\frac{1}{D}\left(\frac{1 - \mu_t A}{\mu_t^2 - \beta^2}\right)\left(\frac{\mu_t + g\mu_\alpha}{\mu_t - g\mu_s}\right) + \frac{2g}{\mu_t'}\right]\mu_s$$
$$\times \exp(-\mu_t L)\tilde{I}(\lambda, \omega).$$

(14b)

For an arbitrary harmonic optical source, which creates the total photon density field $\psi_t(r, z; \omega)$, Eq. (4),

in the turbid medium the thermal-wave field is given by[12]

$$\nabla^2 T(r, z; \omega) - \sigma_t^2(\omega)T(r, z; \omega)$$
$$= -\eta_{NR}(\mu_\alpha/k_t)\psi_t(r, z; \omega), \quad (15a)$$

where

$$\sigma_t(\omega) = \sqrt{i\omega/\alpha} \qquad (\mathrm{m}^{-1}) \quad (15b)$$

is the thermal wave number, α is the thermal diffusivity $(\mathrm{m}^2\ \mathrm{s}^{-1})$, and k_t is the thermal conductivity $(\mathrm{Wm}^{-1}\ \mathrm{K}^{-1})$ of the medium. For generality we assume homogeneous boundary conditions of the third kind[12,15] at both interfaces $(0, L)$:

$$-k_t \hat{\mathbf{n}} \cdot \nabla T(r, z; \omega)|_{z=0,L} = hT(r, z; \omega)|_{z=0,L}. \quad (16)$$

Here $\hat{\mathbf{n}}$ is the outward unit vector normal to the surface at $z = 0, L$; and $h\ (\mathrm{Wm}^{-2}\ \mathrm{K}^{-1})$ is the heat transfer coefficient. For normal incidence,

$$\hat{\mathbf{n}} \cdot \nabla = -\frac{\partial}{\partial z}\bigg|_{z=0}, \quad \hat{\mathbf{n}} \cdot \nabla = \frac{\partial}{\partial z}\bigg|_{z=L}.$$

Taking advantage of the cylindrical symmetry of the exciting Gaussian laser beam, we use the Hankel transformation for the thermal-wave field:

$$\tilde{\tau}(\lambda, z; \omega) = \int_0^\infty T(r, z; \omega)J_0(\lambda r)r\,dr. \quad (17)$$

The Hankel transform of the PTR signal $U(r, \omega)$ can then be written as

$$\tilde{u}(\lambda, \omega) = C \int_{\Lambda_1}^{\Lambda_2} W(\Lambda)\mu_{IR}(\Lambda)d\Lambda \int_0^L \tilde{\tau}(z; \lambda, \omega)$$
$$\times \exp[-\mu_{IR}(\Lambda)z]dz, \quad (18)$$

where Λ denotes wavelength, Λ_1 and Λ_2 are the limits of the spectral bandwidth of the infrared detector, and $W(\Lambda)$ is a wavelength-dependent coefficient involving the Planck distribution function and the spectral response of the detector.[16] C is a constant involving both instrumental factors (e.g., the system transfer function), and the grouping of physical terms

$4\sigma\epsilon T_0^3$ for small thermal-wave amplitudes $|T_{max}| \ll T_0$. T_0 is the ambient temperature, σ is the Stefan–Boltzmann constant $[\sigma = 5.6703 \times 10^{-8}\ \mathrm{W/m^2K^4}]$, and ϵ is the emissivity of the turbid medium. The spectrally averaged Hankel transform $\langle \tilde{u}(\lambda, \omega)\rangle$ is given by

$$\langle \tilde{u}(\lambda, \omega)\rangle = \frac{\tilde{u}(\lambda, \omega)}{\int_{\Lambda_1}^{\Lambda_2} W(\Lambda)d\Lambda}. \quad (19)$$

Using the "effective IR absorption/emission coefficient" definition of Majaron et al. (Ref. 17, p. 114),

$$\langle \mu_{eff}\exp(-\mu_{eff}z)\rangle$$
$$= \frac{\int_{\Lambda_1}^{\Lambda_2} W(\Lambda)\mu_{IR}(\Lambda)\exp[-\mu_{IR}(\Lambda)z]d\Lambda}{\int_{\Lambda_1}^{\Lambda_2} W(\Lambda)d\Lambda}, \quad (20)$$

we can write

$$\langle \tilde{u}(\lambda, \omega)\rangle = C \int_0^L \langle \mu_{eff}\exp(-\mu_{eff}z)\rangle\tilde{\tau}(z; \lambda, \omega)dz$$
$$\cong C\bar{\mu}_{IR} \int_0^L \tilde{\tau}(z; \lambda, \omega)\exp(-\bar{\mu}_{IR}z)dz. \quad (21)$$

Here $\bar{\mu}_{IR}$ is the effective IR absorption coefficient of the medium. Note that the spectrally averaging notation $\langle \cdots \rangle$ was dropped from the second (approximate) version of Eq. (21) and was replaced by an overbar to indicate spatial averaging over the depth coordinate z, in agreement with accepted practice in the analysis of photothermal radiometric signals.[18,19] Majaron et al.[17] have shown that $\bar{\mu}_{IR}$ may depend strongly on probed depth z. Simulations that use a correction algorithm for pulsed-laser PTR of some biomedical materials demonstrated that errors of up to 30% of the signal value may occur when constant $\bar{\mu}_{IR}$ is assumed. Nevertheless, in FD PTR of dental enamels, where relatively large values of $\bar{\mu}_{IR}$ have been obtained (Table 1), they indicate IR absorption and emission depths of the order of 5–33 μm. Within this shallow depth

Table 1. Measurements of Fluorophore Lifetimes (τ_1 and τ_2) from FD LM Phases and Enamel Optical Properties (μ_α, μ_s, $\bar{\mu}_{IR}$) from FD PTR Amplitude and Phase Fits to the Theory[a]

Dental Enamel Parameters	Tooth 1			Tooth 2	Tooth 3	Tooth 4	Tooth 5	Ref. 20 (λ = 400–500 nm)	Ref. 21
	Position 1	Position 2	Position 3						
L (mm)	1.0	1.5	2.0	2.0	2.0	2.0	2.0	0.3	0.003–2.0
τ_1 (ms)	2.00	2.04	2.00	1.6	2.0	2.2	1.9		
τ_2 (μs)	1.00	1.02	1.30	0.22	0.02	<0.01	0.01		
μ_α (cm^{-1})	0.1 ± 0.1	0.1 ± 0.1	0.1 ± 0.1	2.6 ± 0.1	0.1 ± 0.1	0.1 ± 0.1	0.1 ± 0.1	<1	<1
$\bar{\mu}_{IR}$ (cm^{-1})	380 ± 5	300 ± 5	300 ± 5	2200 ± 5	1200 ± 5	400 ± 5	1300 ± 5		
μ_s (cm^{-1})	122 ± 1	150 ± 1	140 ± 1	92 ± 1	400 ± 1	125 ± 1	170 ± 1	40	105 ± 30

[a]Five healthy teeth were examined, and three positions on the occlusal surface of one tooth and the experimental results are from Refs. 20 and 21.

range, an essentially surface localization of the IR emission contribution is expected, compared with the much longer absorption length $1/\mu_\alpha$ of the laser exciting radiation. Furthermore, it is expected[16] that the spectral variation of μ_{eff} can be much reduced at shallow depths, and thus the error committed by use of the approximate Eq. (21) may be much less than 30%. Computationally, an effective value of $\bar{\mu}_{\text{IR}}$ can be extracted over all probed depths from a multiparameter fit of the entire frequency response curve (amplitude and phase) of the turbid medium.

The thermal-wave field in a turbid medium of finite thickness L, such as dental enamel, can be calculated as the solution to the Hankel transform, Eq. (17), of the boundary-value problem described by Eqs. (15) and (16). The procedure is similar to the approach described above on the solution for the Hankel transform of the diffuse photon-density-field boundary-value problem, Eqs. (9) and (10). After considerable algebraic manipulation, and an additional integration over the thickness L as required by Eq. (21), the final expression for the Hankel transform of the backscattered PTR signal is obtained:

$$
\langle \tilde{u}(\lambda, \omega) \rangle = C\bar{\mu}_{\text{IR}} \Bigg\{ B_1 \Bigg[\frac{1 - \exp[-(\beta + \bar{\mu}_{\text{IR}})L]}{\beta + \bar{\mu}_{\text{IR}}}
$$

$$
+ \left[\frac{k_t \beta - h}{1 - \exp(-2qL)} \right]
$$

$$
\times \left(\frac{1 - \exp[-(\bar{\mu}_{\text{IR}} - q)L]}{(h + k_t q)(\bar{\mu}_{\text{IR}} - q)} \{ \exp[-(\beta + q)L] - \exp(-2qL)\} \right.
$$

$$
+ \left. \frac{1 - \exp[-(\bar{\mu}_{\text{IR}} + q)L]}{(h - k_t q)(\bar{\mu}_{\text{IR}} + q)} \{1 - \exp[-(\beta + q)L]\} \right) \Bigg]
$$

$$
+ B_2 \left[\frac{1 - \exp[-(\bar{\mu}_{\text{IR}} - \beta)L]}{\bar{\mu}_{\text{IR}} - \beta} - \left[\frac{k_t \beta + h}{1 - \exp(-2qL)} \right] \right.
$$

$$
\times \left(\frac{1 - \exp[-(\bar{\mu}_{\text{IR}} - q)L]}{(h + k_t q)(\bar{\mu}_{\text{IR}} - q)} \{ \exp[-(q - \beta)L] - \exp(-2qL)\} \right.
$$

$$
+ \left. \left. \frac{1 - \exp[-(\bar{\mu}_{\text{IR}} + q)L]}{(h - k_t q)(\bar{\mu}_{\text{IR}} + q)} \{1 - \exp[-(q - \beta)L]\} \right) \right]
$$

$$
+ B_3 \left[\frac{1 - \exp[-(\bar{\mu}_{\text{IR}} + \mu_t)L]}{\bar{\mu}_{\text{IR}} + \mu_t} + \left[\frac{k_t \mu_t - h}{1 - \exp(-2qL)} \right] \right.
$$

$$
\times \left(\frac{1 - \exp[-(\bar{\mu}_{\text{IR}} - q)L]}{(h + k_t q)(\bar{\mu}_{\text{IR}} - q)} \right.
$$

$$
\times \{ \exp[-(\mu_t + q)L] - \exp(-2qL)\}
$$

$$
+ \frac{1 - \exp[-(\bar{\mu}_{\text{IR}} + q)L]}{(h - k_t q)(\bar{\mu}_{\text{IR}} + q)}
$$

$$
\left. \left. \times \{1 - \exp[-(\mu_t + q)L]\} \right) \right] \Bigg\}, \tag{22}
$$

with the following definitions:

$$
B_1(\lambda, \omega) = \frac{\eta_{\text{NR}}\mu_\alpha}{k_t(\beta^2 - q^2)}\, b_1(\lambda, \omega), \tag{23a}
$$

$$
B_2(\lambda, \omega) = -\frac{\eta_{\text{NR}}\mu_\alpha}{k_t(\beta^2 - q^2)}\, b_2(\lambda, \omega), \tag{23b}
$$

$$
B_3(\lambda, \omega) = -\frac{\eta_{\text{NR}}\mu_\alpha}{k_t(\mu_t^2 - q^2)}\, b_3(\lambda, \omega), \tag{23c}
$$

where, for arbitrary optical source radial distribution $I(r, \omega)$ with Hankel transform $\tilde{I}(\lambda, \omega)$,

$$
b_1(\lambda, \omega) \equiv \frac{1}{H(\lambda, \omega)}\, [-F_1 + \gamma F_2 \exp(-\beta L)], \tag{24a}
$$

$$
b_2(\lambda, \omega) \equiv \frac{1}{H(\lambda, \omega)}\, [F_2 - \gamma F_1 \exp(-\beta L)\exp(-\beta L)], \tag{24b}
$$

$$
b_3(\lambda, \omega) \equiv \left[1 - \frac{\mu_s}{D(\mu_t^2 - \beta^2)} \left(\frac{\mu_t + g\mu_\alpha}{\mu_t - g\mu_s} \right) \right] \tilde{I}(\lambda, \omega), \tag{24c}
$$

$$
H(\lambda, \omega) \equiv (1 + A\beta)[1 - \gamma^2 \exp(-2\beta L)], \tag{24d}
$$

$$
q^2(\lambda, \omega) \equiv \lambda^2 + \sigma_t^2(\omega) \qquad (\text{m}^{-2}). \tag{25}
$$

In the case of a Gaussian laser beam with spot size W and power P, a surface of reflectivity R, and intensity modulation at angular frequency ω, the ac component of $\tilde{I}(\lambda, \omega)$ is given by Eq. (11a). F_1 and F_2 are defined in Eqs. (14); γ is defined in Eq. (13). Depending on the value of h, the two limiting cases of Eq. (22) for $h = 0$ (adiabatic boundaries) and $h \rightarrow \infty$ (diathermal or isothermal boundaries) are obtained immediately.

3. Experimental Method

The experimental setup to perform simultaneous FD PTR and LM studies is shown in Fig. 1. A 488-nm wavelength cw Innova 100 Ar$^+$ laser from Coherent was modulated by an external acousto-optic modulator at frequency $f = \omega/2\pi$, where ω is the angular modulation frequency. The laser beam was then focused with a high-performance lens onto a sample to a radial ($1/e^2$) spot size of approximately 30 μm. The incident power was <20 mW. The backscattered blackbody radiation from the optically excited sample was collected, collimated, and focused onto a liquid-nitrogen-cooled HgCdTe (mercury–cadmium–telluride) detector by two axially aligned reflecting objectives. The HgCdTe detector had an active square size area of 50 μm × 50 μm and a spectral bandwidth of 2–12 μm. An antireflection-coated germanium window with a transmission bandwidth of 2–14 μm was mounted in front of the detector to block any visible radiation

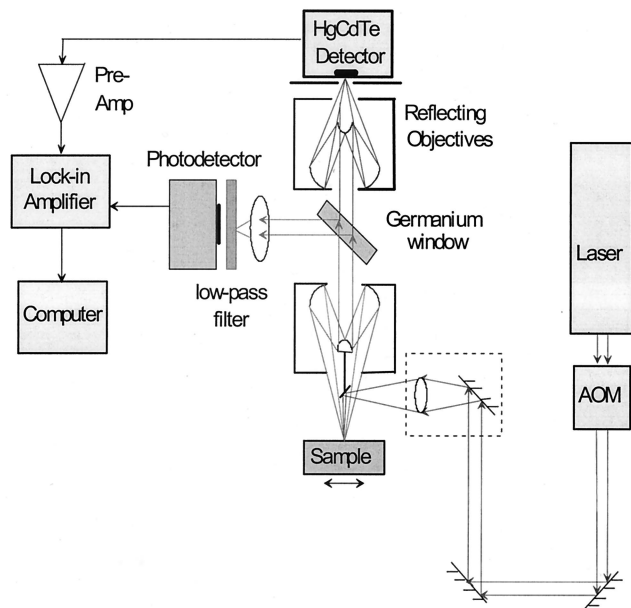Fig. 1. Schematic of the FD PTR and LM imaging instrumentation. AOM, acousto-optic modulator.

Fig. 2. Side view cross section of a dentin–enamel interface of an extracted molar.

from the pump laser. Before it was sent to the digital lock-in amplifier, the photothermal radiometric signal was amplified by a preamplifier with a frequency bandwidth of dc −1 MHz. The process of data acquisition and storage was automated. For the simultaneous measurement of LM and PTR signals, a germanium window was placed between the path of the two reflective objectives. The germanium window was utilized so that wavelengths above the Ge bandgap would be reflected, whereas the subbandgap IR radiation would be transmitted to the second reflecting objective, which was focused onto the IR detector. The LM signal was focused onto a photodetector with a spectral bandwidth of 300 nm–1.1 μm. A cutoff colored glass filter was placed in front of the photodetector to suppress scattered laser light, and the spectrally integrated enamel LM following excitation by the 488-nm laser light was monitored. To test if any experimental components emitted fluorescence, a measurement with a mirror as a sample was performed. No LM signal could thus be detected. The experiments we performed in this study were dynamic, generating local depth-dependent information by scanning the laser beam modulation frequency (a frequency scan) in both PTR and LM modes. The objectives of the experimental research were to obtain optical properties of dental enamel from PTR amplitude and phase frequency scans through use of relaxation lifetime parameters obtained from modulated LM scans.

4. Experimental Results

To study the dynamic nature (i.e., signal dependence on modulation frequency) of dental enamel with reasonable signal-to-noise ratio, both LM and
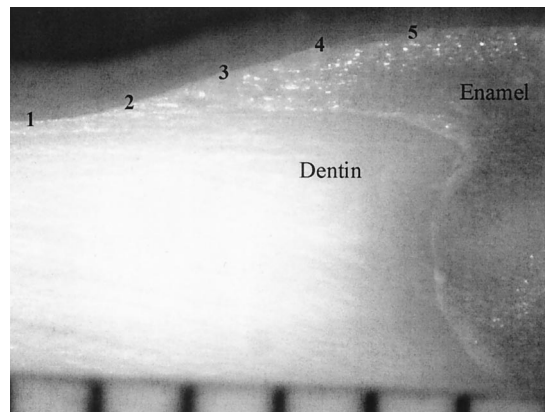
PTR frequency scans were performed at various positions along a dentin–enamel interface of a cross-sectioned extracted molar (tooth 1) as shown in Fig. 2 in the range of 10 Hz–10 kHz. Position 1 is dentin, position 2 is enamel of 0.5-mm thickness over the dentin, position 3 is enamel of 1-mm thickness, position 4 is enamel of 1.5-mm thickness, and position 5 is 2-mm-thick enamel. Figure 3 shows the simultaneous PTR and LM frequency scans for these five positions. Dentin (1) exhibits low LM amplitude [Fig. 3(a)] as compared with the approximately thermally semi-infinite enamel (4 and 5). For positions 3–5 the PTR (as well as the simultaneously obtained LM) frequency responses do not extend beyond 2–3 kHz, owing to the low and noisy PTR signal-to-noise ratios obtained from these and other healthy enamels above this frequency range. Positions 2 and 3 show a progression in LM ampli-
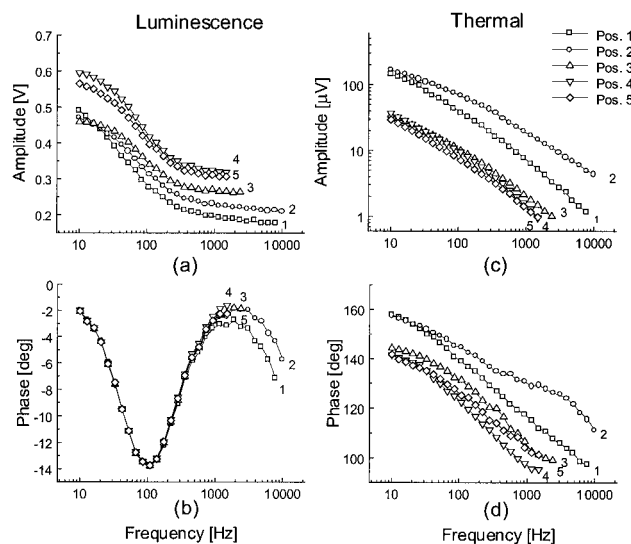

Fig. 3. Simultaneous FD LM and PTR frequency responses at five locations as marked in Fig. 2. Location 1, pure dentin; locations 2–5, increasingly thicker enamel overlayers on dentin (see text). (a) LM amplitude scan; (b) LM phase scan; (c) PTR amplitude scan; (d) PTR phase scan.

tude increase over increasingly thicker enamel layers. The accompanying PTR amplitudes exhibit inversion of signal order from positions 1 and 2 because of thermal-wave confinement within the thin enamel layer, which tends to decrease for thicker enamel layers.[12] Thermal-wave confinement occurs within regions or layers of uniform thermal properties, which terminate at abrupt interfaces and boundaries with layers of different (usually poorer) thermal properties. The spatially superposed forward-diffusing and interface-accumulated thermal-wave power results in the appearance of an increased signal phase (node), which is evidenced in curve 2. At position 2, the sublayer of dentin below the enamel (of lower thermal conductivity and diffusivity than enamel[22]) causes the thermal-wave confinement that can be clearly seen as a local extremum in the phase. This demonstrates the depth profilometric nature of PTR dental signals. At the low-frequency end, the LM amplitudes of curves 2 and 3 overlap with the dentin level (1), as does the PTR amplitude of 2. Curves 4 and 5 exhibit higher LM amplitude and are almost fully overlapped within experimental error. Error bars are of the size of the various symbols used in Fig. 3. Similar signal saturation effects are observed for curves 3, 4, and 5 throughout the PTR amplitude scans. These facts suggest that LM amplitudes from enamel thicknesses $\gtrsim 1.5$ mm and PTR amplitudes from thicknesses $\gtrsim 1$ mm are probing essentially semi-infinite enamel. The LM phase does not show any apparent differences among the various locations up to 1 kHz. At higher frequencies there are some small variations, notably from pure dentin (1). The PTR phase contains more detailed information. Curves 1 and 2 exhibit relatively large amplitudes and clearly separated phases from the remaining curves. A combination of FD PTR and FD LM frequency scans can thus be useful for clinical applications because the presence or thinning of enamel can be determined within affected depths $\lesssim 1.5$ mm below the surface.

5. Multiparameter Fit Methodology

The theoretical model in Section 2 was used to perform multiparameter fits for the LP and photothermal signals obtained from enamel. Although all parameters in Eq. (2) were fitted to the LM amplitude and phase data, the only material parameters of importance were the two characteristic lifetimes τ_1 and τ_2 because the theoretical fit can extract absolute values of these lifetimes. The fitted values of the remaining parameters are either related to the experimental system (W_j and I_0) or are relative values (E_{0j}). Other parameters for the PTR fits were the absorption μ_α, mean IR $\bar{\mu}_{IR}$, and scattering μ_s coefficients. To obtain a fit for the PTR signal, a best fit for the LM signal, Eq. (2), was first investigated. The extrema in the LM phase data such as those of Fig. 3(b) were sensitive to the two lifetimes, and thus we obtained simultaneous fits

for the phase and amplitude by varying each parameter τ_1 and τ_2 independently to provide optimal best fits for both signal channels. Trends obtained from the simulations provided a sense of direction with regard to lifetime values in which the best fit would be found. The two lifetimes were then used as constants in the PTR signal fittings. For healthy teeth, such as that investigated in Fig. 2, the shorter lifetime τ_2 was found to depend on whether enamel or dentin was probed. τ_2 was also found to depend on laser fluence, as expected from a chromophore's optical-level saturation mechanism. At the low laser fluence used in the current experiments, no optical saturation effects could be observed. At present, extensive investigations of the dependence of τ_2 values on the carious state of teeth and on their variance across a range of healthy enamels are under way.

We next fitted the PTR signals by varying the three optical coefficients μ_α, $\bar{\mu}_{IR}$, and μ_s. The enamel thermal parameters, thermal conductivity $k = 0.9$ W/mK, and thermal diffusivity $\alpha = 4.2 \times 10^{-7}$ m^2/s were taken from Ref. 22. We performed simulations of the theoretical model by varying each optical coefficient individually, while the remaining coefficients were kept constant. Trends from these simulations provided information on the relation of these fitting parameters and their tendencies to change the signal output: An increase in the absorption coefficient μ_α increases the phase (i.e., decreases the phase lag) at low frequencies. An increase in the mean IR absorption and emission coefficient $\bar{\mu}_{IR}$ increases the signal at high frequencies. An increase in the scattering coefficient μ_s decreases the signal in the midfrequency range. The heat-loss term h was considered in the theoretical model to account for any heat losses at the interface, including convection and radiation heat transfer to the surroundings. Simulations were performed in which h was varied, and the remaining parameters were kept constant. This term was found (as expected) to provide a best fit when kept constant for all tooth samples and all positions on a given tooth. Finally, we obtained global best fits for the amplitude and phase PTR signals by using a three-dimensional least-residual analysis as outlined below. This procedure can be considered to be the three-dimensional FD generalization of existing two-dimensional time-domain schemes, such as that used with pulsed PTR of turbid media.[8]

The obtained sets of the three optical coefficients μ_α, $\bar{\mu}_{IR}$, and μ_s were examined in terms of their uniqueness. The convection term h was kept constant for all data sets, and the characteristic chromophore lifetimes associated with hydroxyapatite[5] were determined from the LM phase signals. We constructed a three-dimensional contour by plotting μ_α and μ_s on the x and y axes as a function of the least residuals on the z axis. The residuals are the sums over the frequency scans of the theoretical data minus the experimental data squared. Several level surfaces were plotted on the same set of
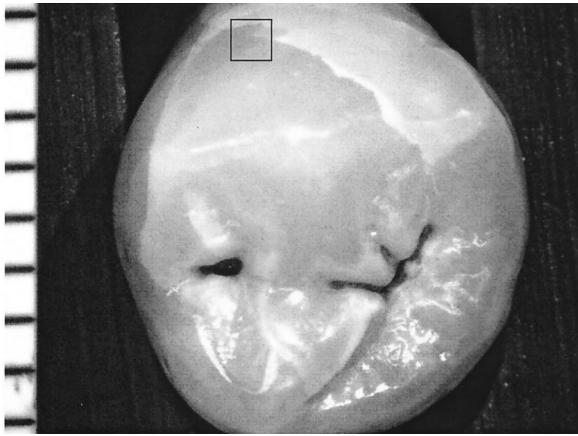
Fig. 4. Top view of a tooth with healthy enamel (tooth 2). The boxed region shows the region from which the data in Fig. 5 were collected.

axes for different values of $\bar{\mu}_{IR}$. These plots showed that, among these surfaces, there was an absolute local minimum. The values obtained from this contour constituted the best fit. We found the optimal value for the mean cosine of the scattering angle g by repeating the foregoing minimization procedure for several values of g until the minimum of the absolute local minima was obtained. We performed a search for another neighboring minimum region by varying μ_α and μ_s on the x and y axes. This search showed that the obtained solution of fitting parameters is a unique set, as there were no other neighboring minima to be found.

6. Multiparameter Fits to Experimental Data from Dental Enamel

To illustrate the fitting procedure, several extracted healthy teeth were studied. We further examined the enamels histologically through cross sectioning after the LM and PTR study was concluded, and they were found to be completely healthy (complete absence of demineralization). The photograph of the occlusal surface of one healthy tooth (tooth 2 in Table 1) is shown in Fig. 4. Data were obtained from inside the region marked by a box. The best fits for both LM and PTR signals are shown in Fig. 5. Equation (1) was used for the fittings of the LM signal. The optimal value of the mean cosine of the scattering angle g determined for all the fits was 0.96. This value is consistent with the range $0.6-0.98$ of g values characteristic of tissues.[23] Equation (22), in the semi-infinite limit, was used to fit the PTR signal for intact enamel, which was thermally semi-infinite (≥ 1 mm thick). Figure 6 shows the three-dimensional (μ_α, $\bar{\mu}_{IR}$, μ_s) contour for three values of $\bar{\mu}_{IR}$ (1900, 2200, and 2700 cm^{-1}). The contours are only partial so as not to obstruct the view. The value $\bar{\mu}_{IR} = 2200$ cm^{-1} gives a contour map where the least residuals are minimal, and hence the minimum located in this contour map is
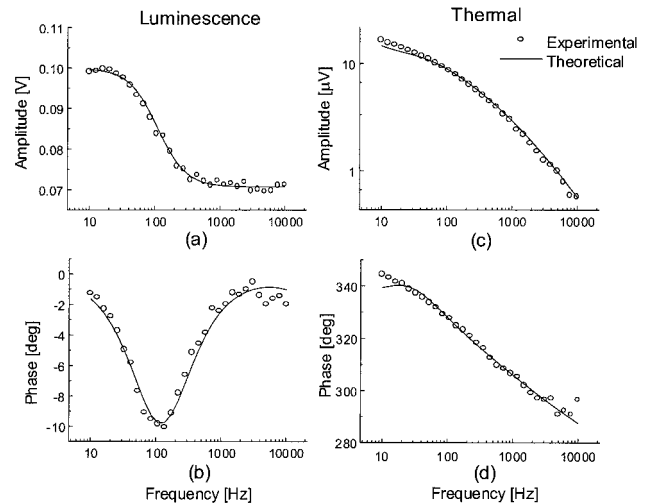

Fig. 5. LM and PTR frequency response from healthy intact enamel (tooth 2). (a) LM amplitude scan; (b) LM phase scan; (c) PTR amplitude scan; (d) PTR phase scan. Fitting parameters for the LM signal were $\tau_1 = 1.6$ ms, $\tau_2 = 0.22$ μs, $N_{T_1} = 919$, $N_{T_2} = 5 \times 10^4$, $W_1 = 10$ s^{-1}, $W_2 = 3.2$ s^{-1}. Fitting parameters for the PTR signals were $\mu_\alpha = 2.6$ cm^{-1}, $\bar{\mu}_{IR} = 2200$ cm^{-1}, $\mu_s = 92$ cm^{-1}, $h = 1 \times 10^7$ W/m^{2}K, $\alpha = 4.2 \times 10^{-7}$ m^2/s, $k = 0.9$ W/mK, $g = 0.96$.

the optimal solution. The best-fitted optical parameters for the healthy enamel are shown in Table 1. The same fitting methodology was applied for several positions of semi-infinite enamel of another extracted healthy tooth (tooth 1), along with three other healthy teeth (3–5), and the results are also listed in Table 1. The actual enamel thicknesses are indicated in Table 1. In general, the optical absorption and scattering values are within documented values measured by means of other methods.[20,21,24] Spitzer and ten Bosch measured diffuse transmission and reflection values of thin tissue slabs in an integrating sphere.[20] In addition, Fried *et al.* measured angulary resolved scattering distributions using a rotating goniometer and deduced scattering and absorption coefficients by comparing measured scattering data with Monte Carlo
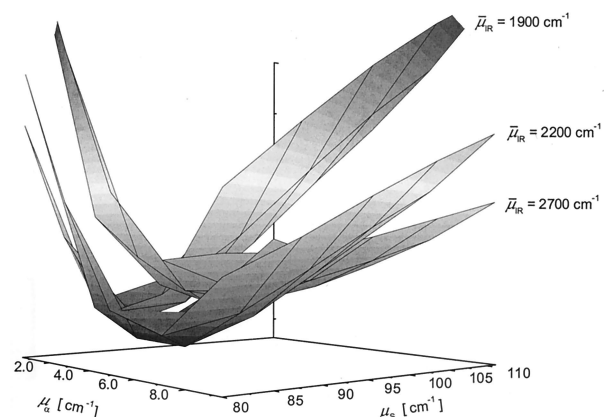

Fig. 6. Three-dimensional contour for optimal solution set (μ_α, μ_s, $\bar{\mu}_{IR}$) for the healthy enamel of tooth 2.

light-scattering simulations.[21] The results from these investigations are shown in Table 1. It is worth mentioning that there exist strong inconsistencies in literature values concerning the optical properties of enamel, with a typical error for the scattering coefficient being ~30%, which may be representative of sample-to-sample variability[21] or because of limitations in technique reliability and precision. It should be noted that our multivariate methodology produces much smaller standard deviations in the measurement of the absorption and scattering coefficients.

These variations in scattering may also be due to the alignment of the enamel rods or prism structure in each sample. The basic microscopic component of enamel is a mineralized rod of hydroxyapatite. The rods range from 4 to 7 μm, originate at the dento–enamel junction, and follow a tortuous path through the inner two thirds of enamel before arriving at their parallel alignment in the outer third of enamel. The complex decussation, in which groups of rods spiral about each other, produces an optical artifact known as Hunter–Shreger bands.[25] These bands can be seen faintly around position 5 of Fig. 2 as vertical striations from the outer surface of the enamel down to the dento–enamel junction. The bands represent enamel rods cut in a plane longitudinal or transverse and oblique to the long axis of the rods. Light transmission is affected by the plane of the section and produces alternating light and dark bands. This phenomenon is particularly marked in the cusp region where it is referred to as gnarled enamel.[26]

7. Conclusions

Quantitative FD infrared PTR and LM were used as complementary nondestructive, nonintrusive methods, the combination of which can yield quantitative values of optical and fluorophore parameters of sound enamel for the first time to our knowledge. Unique sets of the optical parameters (μ_α, μ_s, $\bar{\mu}_{IR}$) of enamel and its fluorophore relaxation time constants (τ_1, τ_2) were obtained by three-dimensional modulated LM and PTR models and a three-dimensional photothermal multiparameter fit formulation and input from FD LM and FD PTR data with respect to fluorophore excited-state lifetimes and optical parameters, respectively. The diagnostic potential of the study is obvious toward the generation of a quantitative band of values for healthy enamel with respect to these parameters so as to provide an explicit criterion for the assessment of healthy enamel and to facilitate the diagnosis of the onset of demineralization in dental enamel.

References

1. C. Longbottom, "Caries detection—current status and future prospects using lasers," in *Lasers in Dentistry VI*, J. D. B. Featherstone, P. Rechmann, and D. Fried, eds., Proc. SPIE **3910,** 212–218 (2000).
2. V. D. Rijke and J. J. ten Bosch, "Optical quantification of caries like lesions in vitro by use of fluorescent dye," J. Dent. Res. **69,** 1184–1187 (1990).
3. K. Konig, H. Schneckenburger, and R. Hibst, "Time-gated in vivo autofluorescence imaging of dental caries," Cell Mol. Biol. **45,** 233–239 (1999).
4. K. Konig, G. Flemming, and K. Hibst, "Laser-induced autofluorescence spectroscopy of dental caries," Cell Mol. Biol. **44,** 1293–1300 (1998).
5. L. Nicolaides, A. Mandelis, and S. H. Abrams, "Novel dental dynamic depth profilometric imaging using simultaneous frequency-domain infrared photothermal radiometry and laser luminescence," J. Biomed. Opt. **5,** 31–39 (2000).
6. A. Mandelis, L. Nicolaides, C. Feng, and S. H. Abrams, "Novel dental depth profilometric imaging using simultaneous frequency-domain infrared photothermal radiometry and laser luminescence," in *Biomedical Optoacoustics*, A. Oraevsky, ed., Proc. SPIE **3916,** 130–137 (2000).
7. A. J. Welch and M. J. C. van Gemert, eds., *Optical-Thermal Response of Laser-Irradiated Tissue* (Plenum, New York, 1995).
8. S. A. Prahl, A. I. Vitkin, U. Bruggemann, B. C. Wilson, and R. R. Anderson, "Determination of optical properties of turbid media using pulsed photothermal radiometry," Phys. Med. Biol. **37,** 1203–1217 (1992).
9. A. Mandelis and C. Feng, "Frequency-domain theory of laser infrared photothermal radiometric detection of thermal waves generated by diffuse-photon-density wave fields in turbid media," Phys. Rev. E (to be published).
10. A. Ishimaru, *Wave Propagation and Scattering in Random Media* (Academic, New York, 1978.
11. A. Ishimaru, Y. Kuga, R. L.-T. Cheung, and K. Shimizu, "Scattering and diffusion of a beam wave in randomly distributed scatterers," J. Opt. Soc. Am. **73,** 131–136 (1983).
12. A. Mandelis, *Diffusion-Wave Fields: Mathematical Methods and Green Functions* (Springer, New York, 2001).
13. R. R. Anderson, H. Beck, U. Bruggemann, W. Farinelli, S. L. Jacques, and J. Parrish, "Pulsed photothermal radiometry in turbid media: internal reflection of backscattered radiation strongly influences optical dosimetry," Appl. Opt. **28,** 2256–2262 (1989), Eq. (8).
14. R. A. J. Groenhuis, H. A. Ferwerda, and J. J. T. Bosch, "Scattering and absorption of turbid materials determined from reflection measurements. 1: theory," Appl. Opt. **22,** 2456–2462 (1983).
15. M. N. Osizik, *Boundary Value Problems of Heat Conduction* (Dover, New York, 1968).
16. J. Vanniasinkam, A. Mandelis, M. Munidasa, and M. Kokta, "Deconvolution of surface and direct metastable-state blackbody emission in Ti:sapphire laser materials using boxcar time-domain photothermal radiometry," J. Opt. Soc. Am. B **15,** 1647–1655 (1998).
17. B. Majaron, W. Verkruysse, B. S. Tanenbaum, T. E. Milner, and J. S. Nelson, "Pulsed photothermal profiling of hypervascular lesions: some recent advances," in *Lasers in Surgery: Advanced Characterization, Therapeutics and Systems X*, R. R. Anderson, K. E. Bartels, L. S. Bass, C. G. Garrett, K. W. Gregory, N. Kollias, H. Liu, R. S. Malek, G. M. Peavy, H.-D. Reidenbach, L. Reinisch, D. S. Robinson, L. P. Tate, Jr., E. A. Towers, and T. A. Woodward, eds., Proc. SPIE **3907,** 114–125 (2000).
18. W. P. Leung and A. C. Tam, "Techniques of flash radiometry," J. Appl. Phys. **56,** 153–161 (1984).

19. R. E. Imhof, B. Zhang, and D. J. S. Birch, "Photothermal radiometry for NDE," in *Non-Destructive Evaluation*, Vol. 2 of Progress in Photothermal and Photoacoustic Science and Technology, A. Mandelis, ed. (Prentice-Hall, Englewood Cliffs, N.J., 1994), Chap. 7, pp. 185–236.

20. D. Spitzer and J. J. ten Bosch, "The absorption and scattering of light in bovine and human dental enamel," Calcif. Tissue Res. **17,** 129–137 (1975).

21. D. Fried, R. E. Glena, J. D. B. Featherstone, and W. Seka, "Nature of light scattering in dental enamel and dentin at visible and near-infrared wavelengths," App. Opt. **34,** 1278–1285 (1995).

22. M. Braden, "Heat conduction in normal human teeth," Arch. Oral Biol. **9,** 479–486 (1964).

23. W. M. Star and J. P. A. Marijnissen, "New trends in photobiology light dosimetry: status and prospects," J. Photochem. Photobiol. B **1,** 149–159 (1987).

24. J. R. Zijp, J. J. ten Bosch, and R. A. J. Groenhuis, "HeNe-laser light scattering by human dental enamel," J. Dent. Res. **74,** 1891–1898 (1995).

25. J. W. Osborn, "The nature of Hunter-Shreger bands in enamel," Arch. Oral Biol. **10,** 929–933 (1965).

26. A. J. Gwinnett, "Structure and composition of enamel," J. Oper. Dent. **17,** Suppl. 5, 10–17 (1992).